

Hydrodynamic and debris-damming failure of bridge decks and piers in steady flow

Oudenbroek, Kevin; Naderi, Nader; Bricker, Jeremy D.; Yang, Yuguang; van der Veen, Cor; Uijtewaal, Wim; Moriguchi, Shuji; Jonkman, Sebastiaan N.

DOI

[10.3390/geosciences8110409](https://doi.org/10.3390/geosciences8110409)

Publication date

2018

Document Version

Final published version

Published in

Geosciences (Switzerland)

Citation (APA)

Oudenbroek, K., Naderi, N., Bricker, J. D., Yang, Y., van der Veen, C., Uijtewaal, W., Moriguchi, S., & Jonkman, S. N. (2018). Hydrodynamic and debris-damming failure of bridge decks and piers in steady flow. *Geosciences (Switzerland)*, 8(11), Article 409. <https://doi.org/10.3390/geosciences8110409>

Important note

To cite this publication, please use the final published version (if applicable).
Please check the document version above.

Copyright

Other than for strictly personal use, it is not permitted to download, forward or distribute the text or part of it, without the consent of the author(s) and/or copyright holder(s), unless the work is under an open content license such as Creative Commons.

Takedown policy

Please contact us and provide details if you believe this document breaches copyrights.
We will remove access to the work immediately and investigate your claim.

Article

Hydrodynamic and Debris-Damming Failure of Bridge Decks and Piers in Steady Flow

Kevin Oudenbroek ¹, Nader Naderi ¹, Jeremy D. Bricker ^{1,*}, Yuguang Yang ¹, Cor van der Veen ¹, Wim Uijttewaal ¹, Shuji Moriguchi ² and Sebastiaan N. Jonkman ¹

¹ Department of Hydraulic Engineering, Faculty of Civil Engineering and Geosciences, Delft University of Technology, PO Box 5048, 2600 GA Delft, The Netherlands; kevinoudenbroek@msn.com (K.O.); N.Naderi@live.com (N.N.); Yuguang.Yang@tudelft.nl (Y.Y.); C.vanderVeen@tudelft.nl (C.v.d.V.); W.S.J.Uijttewaal@tudelft.nl (W.U.); S.N.Jonkman@tudelft.nl (S.N.J.)

² International Research Institute of Disaster Science, Tohoku University, 468-1 AzaAoba, Aramaki, Aoba-ku, Sendai, Miyagi Prefecture 980-8572, Japan; s_mori@irides.tohoku.ac.jp

* Correspondence: j.d.bricker@tudelft.nl; Tel.: +31-15-278-3187

Received: 9 October 2018; Accepted: 5 November 2018; Published: 9 November 2018



Abstract: In countries with steep rivers, such as Japan and the United States, bridges fail on an annual basis. Bridges on spread footings are especially susceptible to failure by hydrodynamic loading, often exacerbated by debris damming. Here, such failures are investigated via small scale model laboratory experiments and full scale numerical simulations. In the laboratory, lift and drag forces and overturning moment on bridge decks, piers, and deck-pier systems, are measured and compared with threshold of failure criteria used in design guidelines. Effects of debris on lift, drag, and moment, as well as three-dimensional effects, are quantified. Via numerical simulations, flow patterns and free surface behaviour responsible for these forces are investigated, and described in a framework as a function of the water depth, flow speed, deck clearance, and girder height. Results show that current guidelines are non-conservative in some cases. Importantly, failure of both decks and piers can be prevented by strengthening pier-deck connections, or by streamlining decks.

Keywords: bridge; flood; drag; lift; computational fluid dynamics; load cell; force

1. Introduction

Both scour and hydrodynamic force have been shown to be common causes of bridge failure [1–3]. Though bridge pier scour has been the subject of varied and intense research [4], hydrodynamic deck and pier failure is typically over-simplified, and in some cases, not conservative. Hydrodynamic failure is especially critical for bridge piers with spread footings founded upon bedrock, where scour is unlikely to cause pier failure. Hydrodynamic deck failure is possible on all inundated bridges, regardless of the foundation type. This paper investigates existing guidelines for hydrodynamic stability of bridge decks and piers, and identifies conditions in which existing guidelines are conservative and non-conservative.

The Eurocode 1991-1-6 [5] specifies the horizontal force exerted by the flow on a deck or pier by a drag equation with a constant drag coefficient dependent on the cross-sectional shape (1.44 for rectangular, and 0.7 for circular). The US Federal Highway Administration [6] specifies drag, lift, and moment coefficients for bridge decks of various shapes, where these coefficients vary as a function of the bridge deck's relative submergence (called inundation ratio later in this paper). The Australian Bridge Design Standards AS 5100 [7] specifies a lift coefficient dependent on the relative submergence, and a drag coefficient dependent on both the relative submergence and the proximity ratio (how close the deck is to the streambed). However, none of these methods account for variation of the drag and lift

coefficients with three-dimensional effects (interaction between pier and deck) or free-surface effects, especially important because of supercritical flow that occurs over the bridge deck and the hydraulic jump that occurs downstream. Furthermore, debris damming effects [8] also need to be quantified.

Malavasi and Guadagnini [9] performed physical experiments on a fully inundated bridge deck only (neglecting piers). They found that the presence of the free surface and bottom boundary caused drag and lift forces different from what would be expected from an identical geometry in an unbounded flow situation. They parameterized drag and lift coefficients as functions of the inundation ratio, h^* , and deck Froude number, Fr_s , only (Equations (1) and (2), and Figure 1).

$$h^* = (h_u - h_b) / s \tag{1}$$

$$Fr_s = U_u / \sqrt{gs} \tag{2}$$

where h_u is the upstream flow depth, h_b is the distance between the bed and the bottom of the superstructure, s is the height of the superstructure, U_u is the flow speed upstream of the superstructure, and g is the gravitational acceleration.

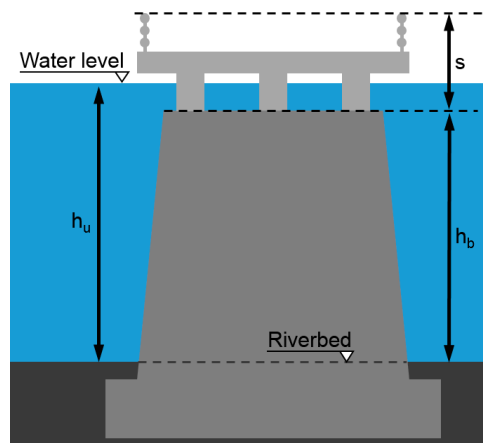


Figure 1. Graphical representation of the variables, h_u , h_b , and s , used in Equations (1) and (2).

Via the use of dynamometers, drag and lift coefficients (Figure 2 shows the definitions of these forces) were calculated by Equations (3) and (4). The highest values of C_D occurred for $h^* = 1.2-1.5$ depending on the deck Froude number, while C_L remained negative (downward force) in all experiments.

$$F_D = C_D \times \rho s U_u^2 / 2 \tag{3}$$

$$F_L = C_L \times \rho s U_u^2 / 2 \tag{4}$$

where F_D is the drag force per unit width, C_D is the drag coefficient, F_L is the lift force per unit width, C_L is the lift coefficient, and ρ is the density of water.

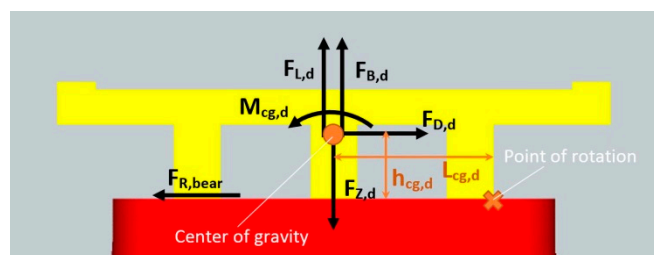


Figure 2. Schematic of forces on the bridge deck. $F_{R,bear}$ is bearing (friction) force. $F_{z,d}$ is weight. $F_{B,d}$ is buoyancy. $F_{L,d}$ is lift. $F_{D,d}$ is drag. $M_{cg,d}$ is the centroidal moment.

Kerenyi et al. [6] distinguished between partially inundated and fully inundated states for their definition of the drag force. Drag and lift coefficients are per Equations (5) and (6). They also measured the centroidal moment (Equation (7)).

$$F_D = \begin{cases} C_D \times \rho U_u^2 / 2 \times s & \text{if } h^* \geq 1 \\ C_D \times \rho U_u^2 / 2 \times h^* s & \text{if } h^* < 1 \end{cases} \quad (5)$$

$$F_L = C_L \times \rho W U_u^2 / 2 \quad (6)$$

$$M_{cg} = C_M \times \rho W^2 U_u^2 / 2 \quad (7)$$

where W is the width of the bridge deck.

Their experiments showed that the drag coefficient had a minimum value ($C_D \sim 0.8$ for a three girder bridge and $C_D \sim 0.7$ for a six girder bridge) at values of h^* ranging from 0.5 to 0.8, while the maximum value ($C_D \sim 1.9$ for a six girder bridge and $C_D \sim 2.2$ for a three girder bridge) occurred at $h^* \geq 1.5$. The drag coefficient of a streamlined cross-section (minimum $C_D \sim 0.2$ and maximum $C_D \sim 1.0$) was lower than blunt cross section shapes. C_L remained negative across all inundation ratios, with lowest values at $h^* = 0.9$ of $C_D = -1.7$ for a three girder bridge, and $C_D = 1.5$ for a six girder bridge. The centroidal moment coefficient, C_M , showed a peak ($C_M = 0.3$ for the six girder deck, and $C_M = 0.25$ for the three girder deck) around a value of h^* equal to 0.8, indicating a stabilizing tendency of the upstream part of the deck to move upwards and the downstream part downwards. As the values of h^* increased, C_M approached a constant value of $C_M = -0.1$ for the three girder deck and $C_M = -0.07$ for the six girder deck, indicating a destabilizing tendency for the upstream edge to rotate upward when deeply submerged.

The Australian Bridge Design Standards [7], based on Jempson [10], parameterize lift and drag coefficients as a function of the relative submergence, $S_r = d_{wgs}/d_{sp}$, and proximity ratio, $P_r = y_{gs}/d_{ss}$, where d_{wgs} is the vertical distance between the upstream water level and deck soffit, d_{sp} is the wetted depth of the upstream side of the deck (including railings), y_{gs} is the vertical distance between the deck soffit and channel floor, and d_{ss} is the wetted depth of the upstream side of the deck (excluding railings). They find that for $S_r < 1$, C_D has a minimum value of 1.3 for $P_r \geq 8$, and a maximum value of $C_D = 2.1$ for $P_r = 1.5$. For $S_r > 1.5$, the minimum C_D is 1.8 for $P_r \geq 8$, and the maximum C_D is 3.3 for $P_r = 1.5$. To be conservative, the Australian Bridge Design Standards specify two lift coefficients, an upper value to be used for calculating deck stability, and a lower value to be used for calculating the required strength of foundations, piers, and girders. The upper values range from $C_L = 0.6$ for $S_r < 1$, to $C_L = 0$ for $S_r > 1.5$. The lower values range from $C_L = -2.0$ for $S_r < 1.5$, to $C_L = -0.8$ for $S_r > 3.0$.

AS5100 [7] also provides design formulas for drag forces on bridges when debris accumulations have formed against them. These formulas have a similar form to Equations (3) and (5). For the area term, the projected area of the debris instead of the bridge should be used. Drag coefficients for both piers and decks are highest ($C_D > 3.0$) for low flow velocities, then decrease as Froude number increases. A distinction is made for the drag forces on the superstructure, where the proximity ratio also has an effect; as P_r increases, the drag coefficient decreases until it reaches a constant value between 0.8 and 1.2 at high values of P_r .

These existing literature and codes are comprehensive, but are lacking in two aspects. One aspect is the three-dimensional behavior of the flow around the full bridge structure (combined pier-deck units), where prior work focused on piers and decks separately. The other aspect that needs further investigation is the effect of combined variation of the Froude number, proximity ratio, and inundation ratio on deck stability, where previous work focused on each of these parameters separately. This also requires quantification of free surface behavior (such as the hydraulic jump that occurs just downstream of a fully inundated deck) on the deck stability.

An example of hydrodynamic bridge failure is the 30 m long Yabitsu Bridge in Iwate, Japan (Figure 3). This bridge collapsed following torrential rainfall on the 9th and 10th of August, 2013. Remnants of the mostly intact bridge deck segments were discovered approximately 50 m downstream.

The bridge piers, also mostly intact, appeared to have toppled over and moved downstream over a distance of several meters. This paper uses the Yabitsu Bridge as a model for an experimental study to determine conditions leading to the threshold of failure of the bridge's decks, piers, and deck-pier system, including the effects of debris damming. A numerical study is then conducted to expand analysis to a broader range of deck geometries and setting heights.



Figure 3. Yabitsu bridge before flood (upper) and after (lower).

2. Materials and Methods

In many situations where bridge decks were inundated during river floods, the bridge substructure (the piers) survived. However, the Yabitsu Bridge suffered total collapse. Two different failure mechanisms that might explain the observed failure are investigated. The first concerns subsequent failure of the bridge deck (superstructure) by sliding or rotation, followed by toppling over of the bridge piers (Hypothesis 1). The second concerns rigid-body failure of the deck-pier system, followed by separation of the sub- and superstructure on impact with the riverbed (Hypothesis 2). The strength of the connection between the bridge deck and bridge pier plays a key role in the failure mechanism that will occur. Considering the extreme of a monolithic connection, Hypothesis 1 will not hold. On the other end of the spectrum, the deck is resting on a frictionless pier; then Hypothesis 2 will not hold.

Experiments were carried out in a closed-system recirculating flume, allowing for independent variation of flow depth and flow velocity. To find the combinations of flow velocity and flow depth at which failure occurs, the experiments consisted of two parts. In the 'free standing experiments', the model bridge deck rested on the model piers by gravity only, relying on friction for its resistance against horizontal movement. The coefficient of friction between the model parts was approximately equal to the friction coefficient between concrete and the material of an elastomeric bearing pad ($\mu = 0.25$) [11]. The strength of the connection between the deck and pier is properly Froude scaled in this way. The

pier was positioned in a recess in a false bottom, mimicking the spread footing foundation (Figure 4). As the anchorage of the pier into the riverbed was accomplished with concrete/grout, it is assumed that this anchorage of the pier in the riverbed had negligible (tensile) strength. Therefore, in the free-standing experiments, the pier was not anchored to the bottom in any way.

The second part of the experiments involved the use of a load cell setup capable of measuring forces in the X-direction (positive downstream) and Y-direction (positive upward) as well as moments in the XY-plane, with a resolution of 0.05 N for force and 0.01 Nm for moment. A stiff steel plate of 4mm thickness was rigidly connected to the measuring surface of the load cell on one end and to the component (bridge deck, bridge pier, or pier-deck system) on the other end (Figures 4 and 5). Small (~1 mm) gaps were left between the components being measured with the load cell and the rest of the setup to prevent spurious force measurement. For more details on the measurement setup, please see Oudenbroek [12].



Figure 4. Laboratory setup, including debris damming on the upstream face of decks. The far deck is outfitted with the load cell, while the other two decks are free standing.

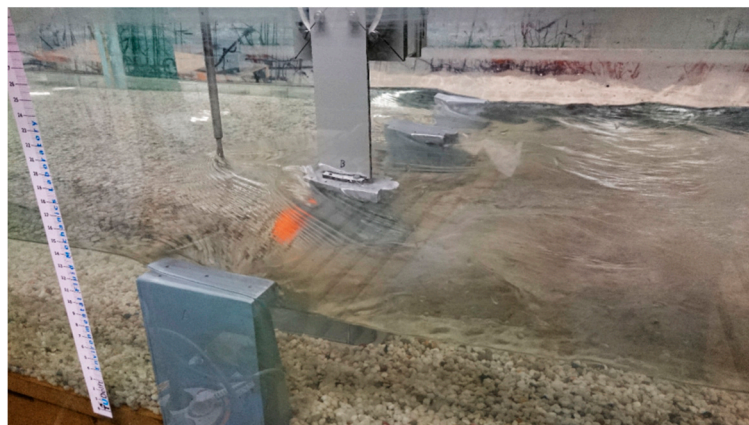


Figure 5. Laboratory setup with one pier connected to the load cell, and the other pier and abutments free standing.

In all experiments, flow depth was estimated via a measure glued to the sides of the transparent glass wall of the flume (Figure 5). Discharge was measured using ultrasonic flow meters in the flume's return flow pipe. Depth-averaged flow velocity was estimated via the discharge and depth measurements. The following failure mechanisms were tested, both for cases without and with debris accumulation:

Hypothesis 1a. *Deck failure; horizontal movement of bridge deck (sliding).*

Hypothesis 1b. *Deck failure; rotation of bridge deck (rolling).*

Hypothesis 1c. *Pier failure; rotation of bridge pier (toppling over).*

Hypothesis 2. *Rotation of pier-deck system (toppling over).*

Both sliding and heaving of the bridge pier and pier-deck system are not considered as possible failure mechanisms because the spread footing foundations of the piers were embedded into the bedrock of the riverbed so lateral movement would be restrained.

Experiments were performed in a flume at a 1:37 geometric scale. For the experiments, plastic scale models of the piers and decks of the Yabitsu Bridge were created (Table 1 and Figure 6). The scale models were hollow plastic and filled with a mixture of lead sheets and sand to achieve the correct Froude-scaled weight distribution. Small gravel was glued to the flume's false bottom to replicate the cobbles of the actual stream bed. Froude scaling was prioritized to guarantee correct scaling of forces on the deck. The model-scale Reynolds number was about 10^4 , compared with a field-scale Reynolds number of 10^6 , both indicating fully turbulent flow in the range of the relatively constant drag coefficient for a sharp-edged bluff body [13]. The model-scale Weber number was approximately 500, indicating that surface tension effects were negligible.

To simulate woody debris, such as logs, sticks, and twigs, circular wooden sticks (debris approximately 0.70 g/cm^3) were glued together to form various shapes. Each stick had a diameter of approximately 1.0 cm. The debris was formed in an attempt to replicate the shape of debris accumulation in its early stages. For the deck, this resulted in the shape shown in Figure 4. Debris dimensions used for damming the pier alone are shown in Table 2, and an example of pier debris damming is shown in Figure 7. Debris conform to the same Froude scaling as the model bridge [12].

Table 1. Dimensions of the scale bridge model (Colors refer to Figure 6).

Bridge Deck (Yellow)	Laboratory Model	Yabitsu Bridge (Actual)
Length (along road axis)	254 mm	9.4 m
Width (along river axis)	142 mm	5.3 m
Height	Girders: 19 mm Deck: 11 mm	Girders: 700 mm Deck: 410 mm
Base of the pier (red)		
Length (along river axis)	Bottom: 127 mm Top: 113 mm	Bottom: 4.7 m Top: 4.2 m
Width (along road axis)	Bottom: 41 mm Top: 49 mm	Bottom: 1.5 m Top: 1.8 m
Height	129 mm	4.8 m
Pier foundation (brown)		
Length (along river axis)	147 mm	5.4 m
Width (along road axis)	61 mm	2.3 m
Height	22 mm	814 mm
Abutment (green)		
Length (along river axis)	96 mm	3.6 m
Width (along road axis)	76 mm	2.8 m
Height	151 mm	5.6 m

$$Fr = U_u / \sqrt{gh_u} \tag{8}$$

Table 3. Flow conditions investigated.

Hypothesis 1—deck—without debris	$h_u = 12.0 \text{ cm to } 20.0 \text{ cm}$	$Fr = 0.33 \text{ to } 0.52$
Hypothesis 1—deck—with debris	$h_u = 13.0 \text{ cm to } 19.0 \text{ cm}$	$Fr = 0.10 \text{ to } 0.52$
Hypothesis 1—pier—without debris	$h_u = 8.0 \text{ cm to } 21.0 \text{ cm}$	$Fr = 0.40 \text{ to } 0.62$
Hypothesis 1—pier—with debris	$h_u = 8.0 \text{ cm to } 17.0 \text{ cm}$	$Fr = 0.34 \text{ to } 0.52$
Hypothesis 2—combination—without debris	$h_u = 12.0 \text{ cm to } 21.0 \text{ cm}$	$Fr = 0.52$
Hypothesis 2—combination—with debris	$h_u = 16.0 \text{ cm to } 21.0 \text{ cm}$	$Fr = 0.52$

3.1.2. Rigidly Connected Deck-Pier System

The ‘free-standing experiments’ were performed first. Collapse of the rigid deck-pier model (Hypothesis 2) was not observed even under the most aggressive flow conditions, and even with exaggerated amounts of simulated debris lodged against the model (Figure 8). The force balance resulting from the ‘load cell experiments’ conducted on the deck-pier system supported this observation (Figure 9). Even though the total drag force increased monotonically as the inundation ratio, h^* , was increased, lift forces on the system became negative (directed downwards) as h^* was increased. The effect of the negative lift forces keeping the free-to-move scale model in place overwhelmed the effect of the drag forces.

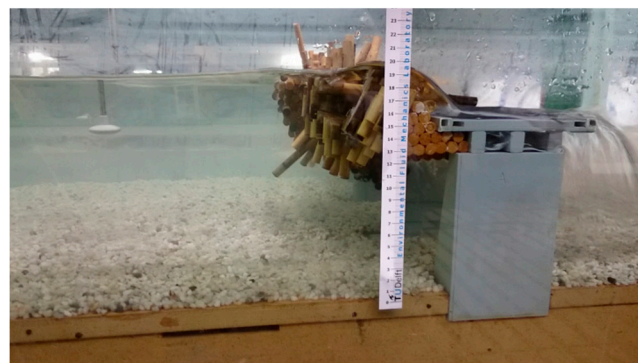


Figure 8. Laboratory setup showing the rigidly connected deck-pier system with excessive debris damming.

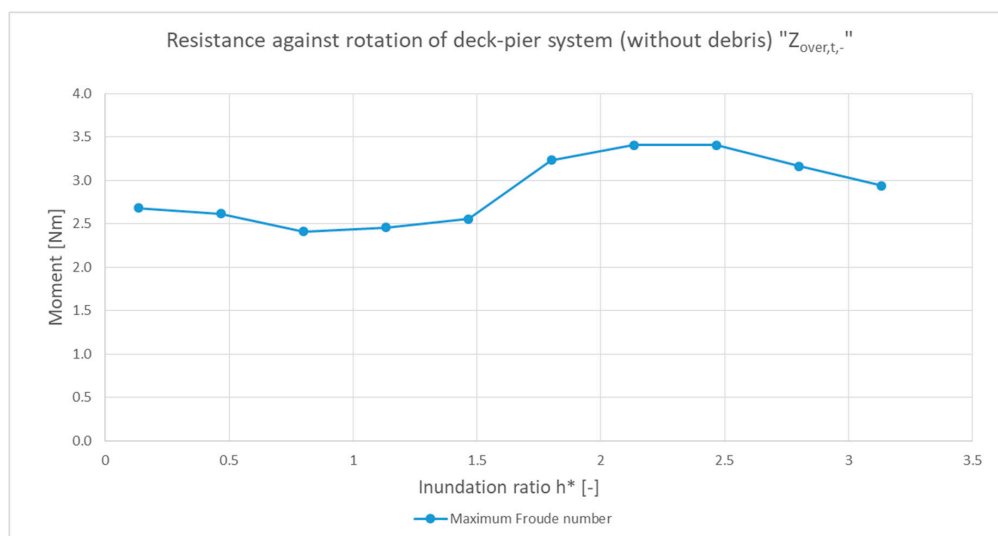


Figure 9. Self-weight restoring moment of the deck-pier system (about the heel of the pier) minus the hydrodynamic overturning moment, as measured by the load cell.

3.1.3. Deck Failure Only (No Failure of Piers)

Since it was clear the deck-pier system could not fail as one unit, separate failure (Hypothesis 1) was investigated in detail. ‘Free-standing experiments’ on the bridge deck without debris were conducted first to find the range of conditions (flow depth and flow velocity, expressed as the inundation ratio and Froude number) under which failure would and would not be observed. These measurements resulted in Figure 10. It can be seen that for the inundation ratio, $h^* > 3.13$, failure of the bridge deck without debris occurred across the full range of tested Froude numbers. As h^* decreases, failure only occurs at increasingly higher Froude numbers, until no failure was observed at $h^* < 2.13$. This shows that the most important driver of deck failure is the inundation ratio. At low inundation ratios of $h^* < 2.13$, acceleration of flow under the bridge deck results in a downward lift force, preventing failure of the deck. Only at larger inundation ratios is this downward lift reduced enough to allow drag forces to push the deck off. These physics will be investigated more via the numerical model later in this paper.

In agreement with Kerenyi et al. [6] and Bricker and Nakayama [2], results from the load cell experiments show that for $h^* > 1.0$, the combination of lift and buoyancy forces on the bridge deck was actually negative, indicating that the net vertical force was directed downward, despite the effects of buoyancy. Moreover, this negative lift force increased as the Froude number increased.

Figure 11 shows a comparison of the measured drag coefficients with Kerenyi et al. [6]. Although it needs to be stressed that these values strictly cannot be compared directly—as the values stated in [6] were derived for $Fr = 0.32$ only—the difference with the measured values is very large. For $h^* < 1.0$, the measured C_D -values are higher than [6], while for $h^* > 1.0$, the measurements indicate lower C_D -values. However, [6] performed their experiments on an isolated bridge deck segment, while the measurements gathered for this research also include the effects of the nearby piers, which add blockage and therefore accelerate the flow locally. Additionally, the geometry of the scale model used in this research was similar, but not identical, to the geometry used by [6]; the aspect ratio (height/width) was smaller for the models used in these experiments (0.21) than in [6] (0.27). Finally, the bridge deck used by Kerenyi et al. [6] had railings, while that used in our experiments did not. Railings have a substantial effect on the definition of C_D (Equation (5)), as the value of the deck height, s , includes the entire railing height, even though the railings are porous and do not function to block all the flow over this height. At large h^* , C_D values from [6] thus use a larger s , resulting in smaller C_D than for our case, while for small h^* (railings not submerged), there is no difference in the definition. At small h^* , another important difference is that the bridge model used in our experiments had a higher Proximity ratio (4.3) than that of [6], where the proximity ratio was a maximum of 3.5 (in [6], the Proximity ratio varied as the water depth was held constant while the deck was moved vertically to investigate multiple values of h^*). Section 3.2 of this paper (below) finds that, in general, a lower Proximity ratio results in more interaction with the streambed, and a higher C_D ; this may be related to the larger values of C_D measured by [6] at small h^* .

		h*	0.13	0.47	0.80	1.13	1.47	1.80	2.13	2.47	2.80	3.13	3.47	3.80
		h _u [cm]	13.0	14.0	15.0	16.0	17.0	18.0	19.0	20.0	21.0	22.0	23.0	24.0
U [cm/s]	50	0.443	0.427	0.412	0.399	0.387	0.376	0.366	0.357	0.348	0.340	0.333	0.326	
	52	0.460	0.444	0.429	0.415	0.403	0.391	0.381	0.371	0.362	0.354	0.346	0.339	
	54	0.478	0.461	0.445	0.431	0.418	0.406	0.396	0.386	0.376	0.368	0.359	0.352	
	56	0.496	0.478	0.462	0.447	0.434	0.421	0.410	0.400	0.390	0.381	0.373	0.365	
	58	0.514	0.495	0.478	0.463	0.449	0.436	0.425	0.414	0.404	0.395	0.386	0.378	
	60	0.531	0.512	0.495	0.479	0.465	0.452	0.439	0.428	0.418	0.408	0.399	0.391	
	62	0.549	0.529	0.511	0.495	0.480	0.467	0.454	0.443	0.432	0.422	0.413	0.404	
	64	0.567	0.546	0.528	0.511	0.496	0.482	0.469	0.457	0.446	0.436	0.426	0.417	
	66	0.584	0.563	0.544	0.527	0.511	0.497	0.483	0.471	0.460	0.449	0.439	0.430	
	68	0.602	0.580	0.561	0.543	0.527	0.512	0.498	0.485	0.474	0.463	0.453	0.443	
	70	0.620	0.597	0.577	0.559	0.542	0.527	0.513	0.500	0.488	0.476	0.466	0.456	
	72	0.638	0.614	0.594	0.575	0.558	0.542	0.527	0.514	0.502	0.490	0.479	0.469	
	74	0.655	0.631	0.610	0.591	0.573	0.557	0.542	0.528	0.516	0.504	0.493	0.482	
	76	0.673	0.649	0.627	0.607	0.589	0.572	0.557	0.543	0.530	0.517	0.506	0.495	
	78	0.691	0.666	0.643	0.623	0.604	0.587	0.571	0.557	0.543	0.531	0.519	0.508	
80	0.708	0.683	0.659	0.639	0.619	0.602	0.586	0.571	0.557	0.545	0.533	0.521		

Figure 10. Results of the free standing deck experiments. Green cells indicate that no deck failure was observed, while red cells mean that failure occurred consistently across repeated tests. Yellow cells indicate critical conditions, i.e., the deck would be stable for some time (a few tens of seconds), but then collapse. Grey cells represent conditions that were above the maximum achievable Froude number or above a realistic inundation ratio. The number in each cell corresponds to the Froude number of that test. Light green and light yellow colors indicate that no specific experiments were conducted at these conditions, but an outcome was predicted based on the outcomes of neighboring experiments.

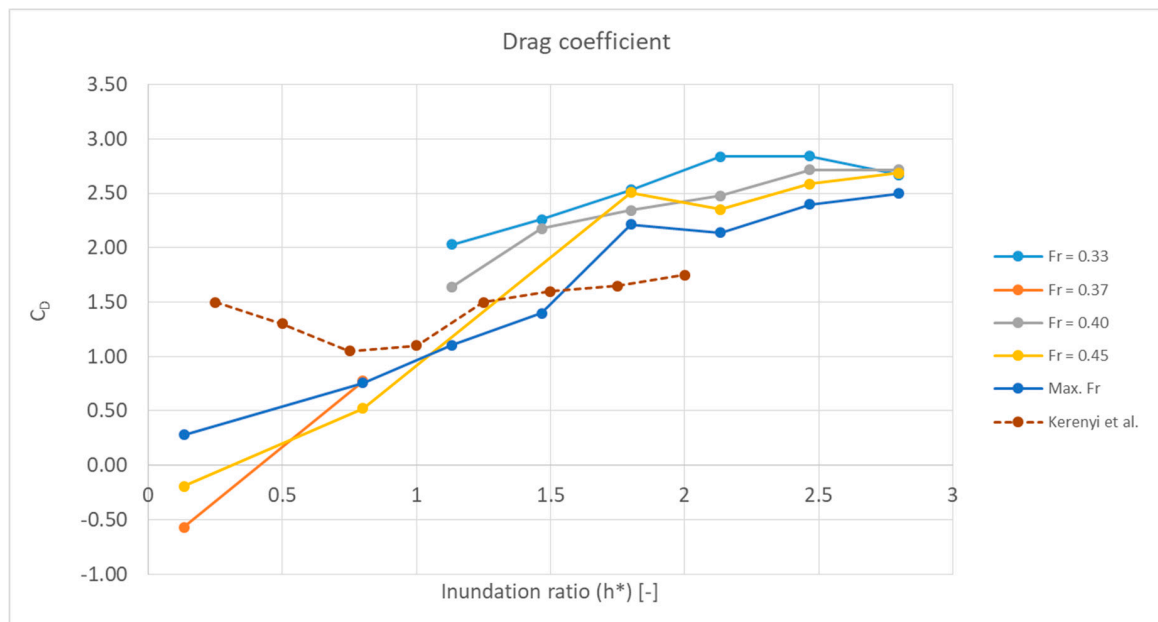


Figure 11. Drag coefficients measured with the load cell, compared with those of the three girder deck of Kerenyi et al. [6]. The dashed line corresponds to the values of Kerenyi et al. [6]. Note that C_D values at $h^* = 0.13$ are based on forces close to the resolution limit of the load cell.

A similar procedure was employed to find the failure conditions of a bridge deck with debris damming, as well as the loads associated with failure. Simulated debris was lodged under the bridge deck and secured in place using fishing wire (Figure 4). This meant that buoyancy forces of the debris were also transferred to the scale model. Identical to the situation without debris, failure was only observed when $h^* > 2.13$, albeit at lower Froude numbers. Failure by sliding occurred for $0.17 < Fr < 0.32$ and failure by overturning was observed for $0.14 < Fr < 0.17$. For $Fr > 0.32$, no failures were observed due to the increasing downward lift force.

3.1.4. Pier Only (after Deck Failure)

For the case of the decks having already been swept away, no collapse of the piers was observed under any of the hydraulic conditions tested without debris. The pier drag coefficient generally increased with Fr , but decreased to the unbounded value of $C_D = 0.7$ [14] with increasing flow depth (Figure 12). Large amounts of simulated debris needed to be introduced into the experiment to observe failure, which only happened under one combination of tested conditions ($h_u = 17.0$ cm; $Fr = 0.34$; Figure 13). Overturning moments as a result of drag increased mostly as a result of a larger flow depth at a constant Froude number, while the Froude number itself did not have a pronounced effect.

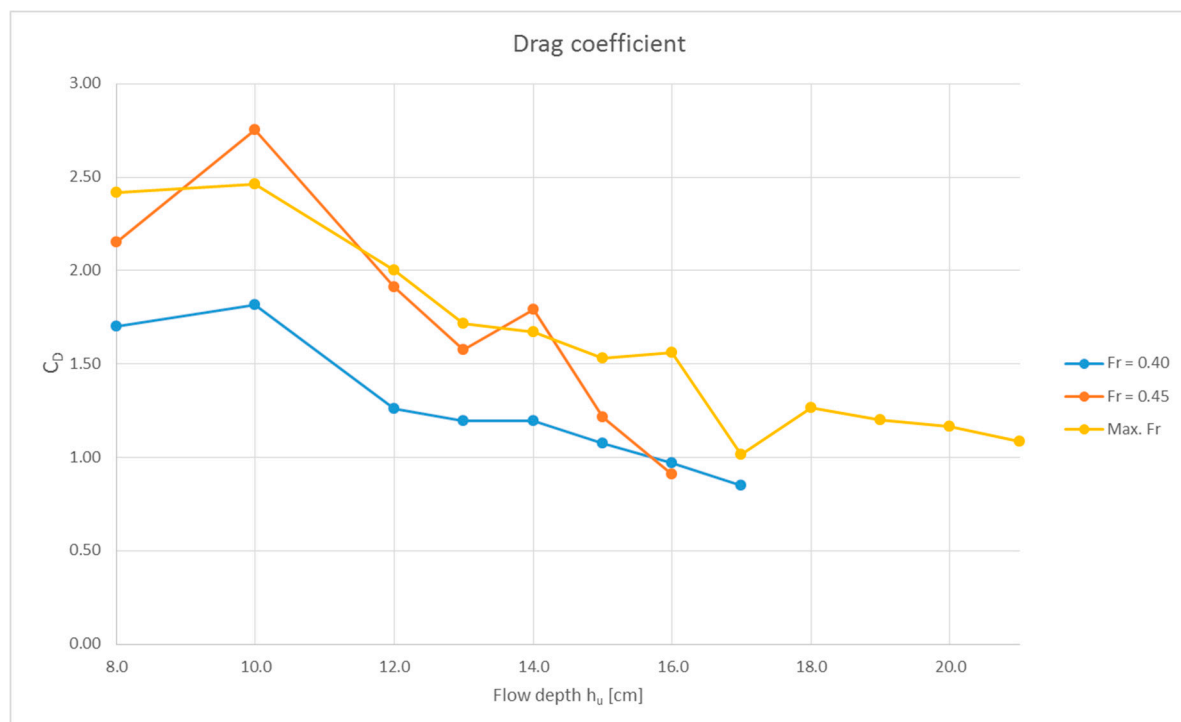


Figure 12. Pier drag coefficients. It can be seen that the values approach the canonical value of 0.7 [14] as the flow depth, h_u , keeps increasing. However, blockage and free surface effects are clearly visible at low flow depths where the pier is not fully submerged.

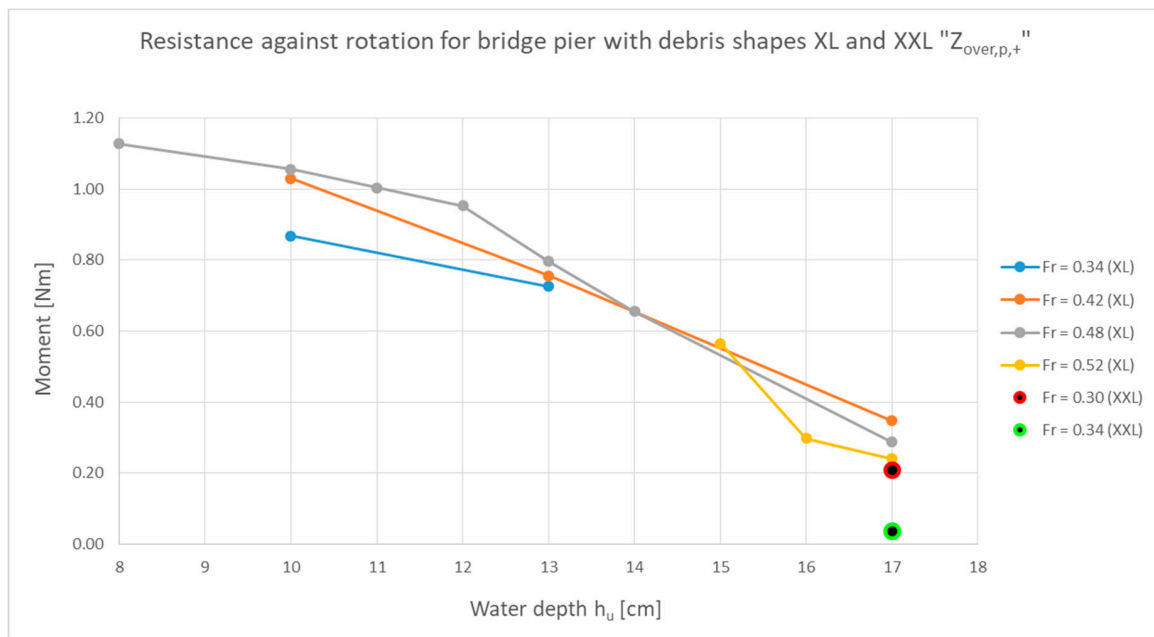


Figure 13. Self-weight restoring moment of the pier (about the heel of the pier) minus the hydrodynamic overturning moment, as measured by the load cell. The only observed failure in the free standing experiments is indicated by the green circle.

3.2. Numerical Simulations

3.2.1. Validation

To assess the flow pattern around the deck, the deck was modeled as a rectangular cylinder (Figure 14). This simple geometry of the deck increases the confidence in the results and gives the chance to systematically assess the changes in flow pattern around the deck. Ansys—Fluent model version 18.2 was used for two-dimensional simulation of the flood—deck interaction. To validate the Fluent model, the simulation results were compared with the results of the physical experiment of Malavasi and Guadagnini [9] at a 1:33 scale. A summary of the experimental conditions used for validation is shown in Table 4.

Table 4. Summary of the experimental conditions used for Fluent model validation.

Flume Length (m)	Deck Length (m)	Deck Thickness, S (m)	h_b (m)	h_u (m)	Fr (—)
5	0.18	0.06	0.14	0.1–0.4	0.1–0.15

The numerical model is built with the same dimension, water depth, and velocity as the experimental condition. As shown in Figure 14, the steady flow rate was defined at the inlet. The outlet was set at a specified water level to keep the desired water level in the flume. The pressure at the top side of the domain was set at atmospheric pressure. The flume bed and bridge were defined with a standard smooth wall function. The K- ω SST turbulence model was assigned as a turbulence model, which performs well in situations where flow separation and an adverse pressure gradient exists [15].

To capture the free surface elevation with higher resolution, the mesh around the free surface level was more finely resolved (Figure 15). The simulation is run for 60 s with the last 20 s of average drag and lift being monitored during the simulation. Table 5 shows the numerical setup.

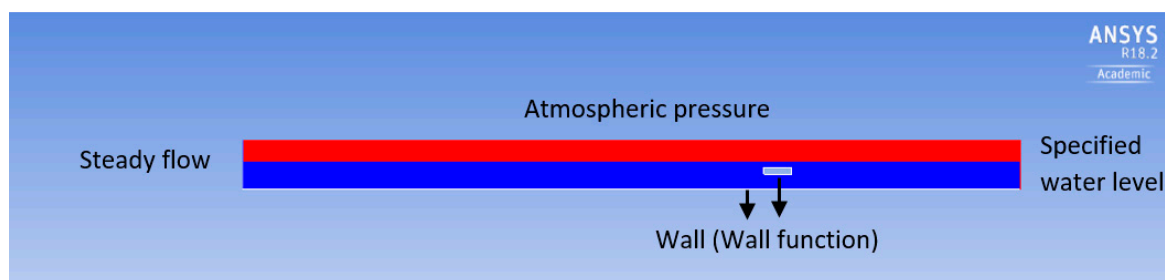


Figure 14. Boundary conditions of the numerical simulation.

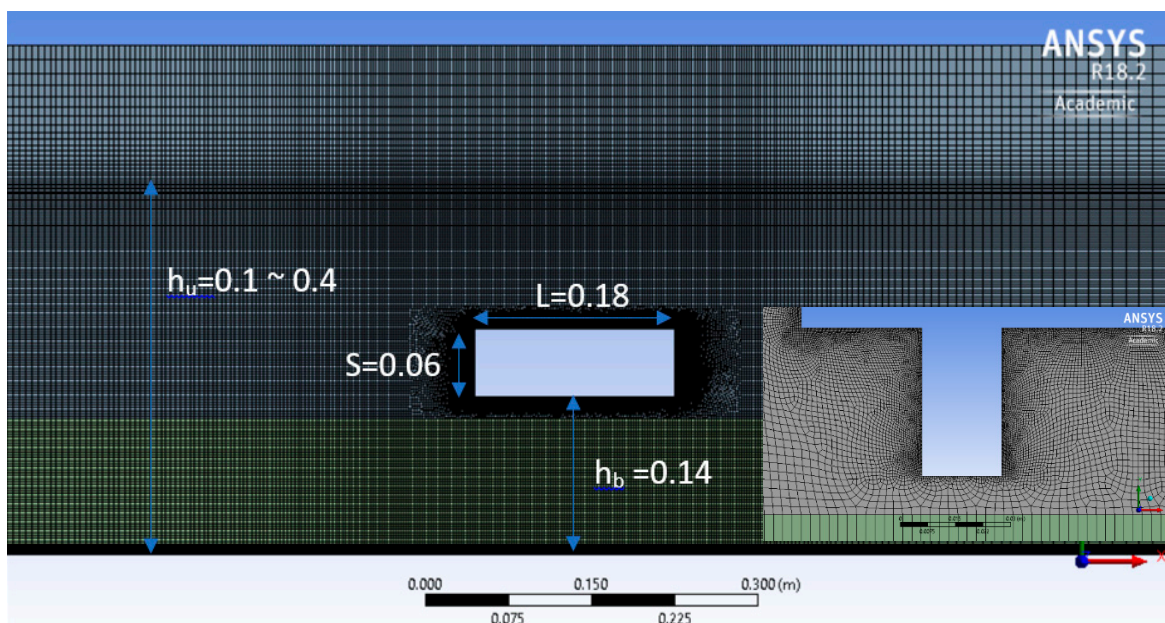


Figure 15. Mesh distribution around the deck. Fine mesh resolution is used near the bridge and at the free surface elevation. Coarser mesh resolution is defined above the free surface where only air exists. Mesh resolution becomes coarser moving away from the deck towards the inlet and outlet. Near the deck, the mesh is flexible quadrilateral, while it is rectangular elsewhere. The inset shows a magnified view of the flexible quadrilateral mesh for the case of the three-girder bridge used in Section 3.2.5 below.

Table 5. Summary of the numerical configuration.

Time step size (s)	0.005
Iteration per time step	20
Multiphase model	Volume Of Fluid (VOF)
Pressure—velocity coupling scheme	Simple
Spatial discretization of momentum, turbulent kinetic energy, and specific dissipation rate	Second order upwind
Under relation factor for pressure	0.3
Under relaxation factors for remaining parameters	0.7
Mesh method/size	Multi-block technique/1 mm–1 cm

The comparison of numerical and experimental results in terms of force coefficients are shown in Figure 16. From this figure, it can be seen that the numerical results strongly agree with the experimental data, proving the capability of the model at calculating forces on submerged objects. As in the laboratory experiments above, the lift coefficient is negative at small values of h^* . This is due to the acceleration of flow under the deck, resulting in lower pressure on the deck’s bottom surface and thus downward lift. As h^* increases, more water is able to flow above the deck as well as below,

thereby negating this effect when the deck is deeply submerged. The drag coefficient, on the other hand, shows a maximum near $h^* = 1$. The reason for this is the definition of C_D in Equation (5) is based on the upstream flow speed, not the local flow speed. Due to the contraction of flow at the bridge deck, which causes maximum blockage near $h^* = 1$, flow accelerates near the deck. Since Equation (5) cannot account for this acceleration, the drag coefficient varies with h^* , but asymptotes to the canonical value for a square cylinder in an unbounded flow of $C_D = 1.6$ at large h^* [16].

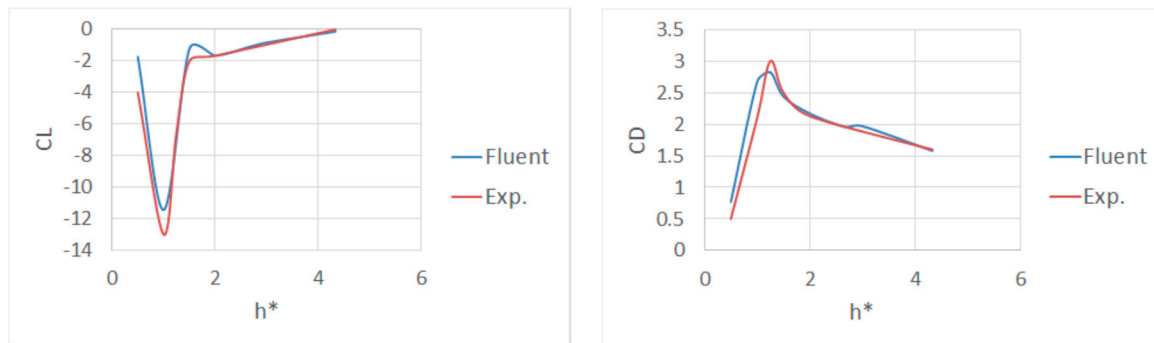


Figure 16. Comparison of numerical and experimental results in terms of force coefficients on the submerged rectangular cylinder.

3.2.2. Effect of Proximity, Blockage, and Inundation Ratios on Bridge Deck Stability

To fully investigate the hydrodynamic loading on a bridge deck, three sets of experiments were performed as shown in Figure 17. Each scenario keeps one geometric ratio constant, while varying the other two and the flow speed.

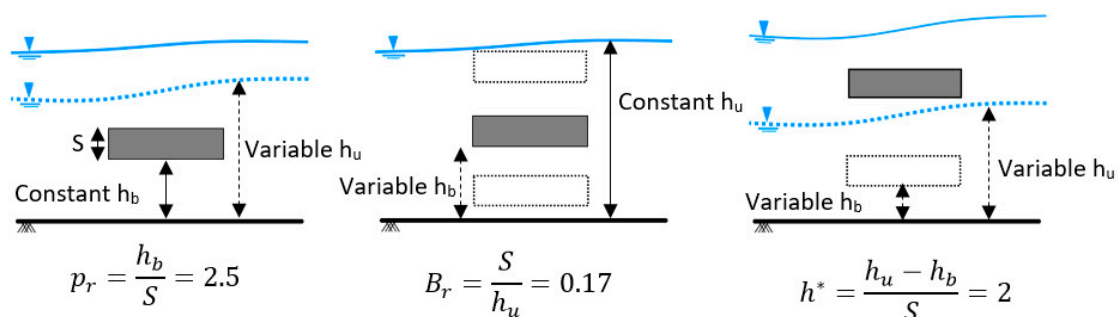


Figure 17. Bridge and water depth configurations. Scenario1 (left picture): Fixed proximity ratio, $p_r = 2.5$. Scenario 2 (middle picture): Constant Blockage ratio, $B_r = 0.17$. Scenario 3 (right picture): Constant inundation ratio, $h^* = 2$.

Scenario 1: Fixed Proximity Ratio

In the first set of experiments, to analyze the effect of the inundation ratio on hydrodynamic forces on the bridge deck, the distance of the channel floor to the bottom of deck was kept at 0.175 m, while the water level was in the range of 0.196 to 0.455 m. The inundation ratio is in the range of $h^* = 0.3$ to 4. To have subcritical flow upstream, the flood velocity was in the range from 0.2 to 0.8 m/s, which is equivalent to a Froude number of 0.09 to 0.58.

The dependence of the drag coefficient on the inundation ratio (h^*) and velocity is shown in Figure 18. There are two distinct trends for $Fr_s \leq 0.5$ and $Fr_s > 0.5$. For $Fr_s \leq 0.5$, the drag coefficient increases with increasing h^* up to an h^* around 1–1.2, after which it starts to drop. The increasing slope of the graph indicates an increase in the inundation of the frontal area of the deck. The decreasing slope indicates a reduction in the blockage ratio (blockage ratio, B_r , is defined as the frontal area of the deck divided by the upstream water depth). However, it is not straightforward to distinguish between the

effect of the blockage ratio and submergence ratio by considering this configuration, i.e., fixed bridge and variable water depth. As the submergence ratio increases, $h^* \geq 3.5$, the drag coefficient approaches the constant value of about 1.6, which is close to the experimental result of the drag coefficient for a rectangular cylinder in an unbounded flow (Yu and Kareem [16]).

When the deck Froude number is larger than 0.6, the maximum peak of C_D occurs at an h^* of around 2. This shift of maximum C_D for higher inundation ratios can be attributed to the occurrence of a hydraulic jump just downstream of the bridge (Figure 19). In this case, the Froude number based on the water depth above the deck becomes supercritical ($Fr > 1$), and a hydraulic jump occurs just downstream of the deck.

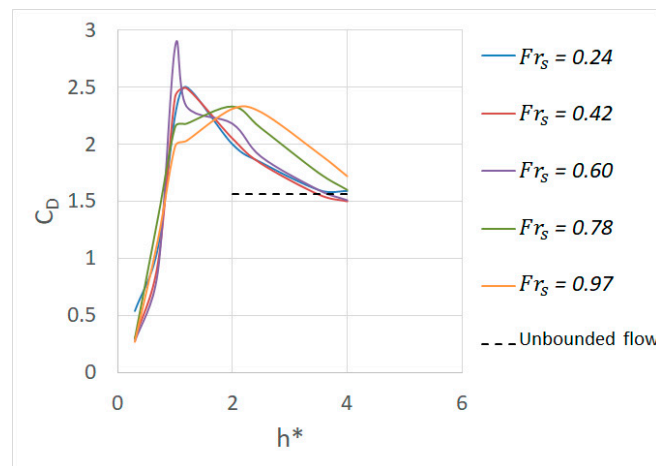


Figure 18. Drag coefficient versus inundation ratio for different upstream velocities.

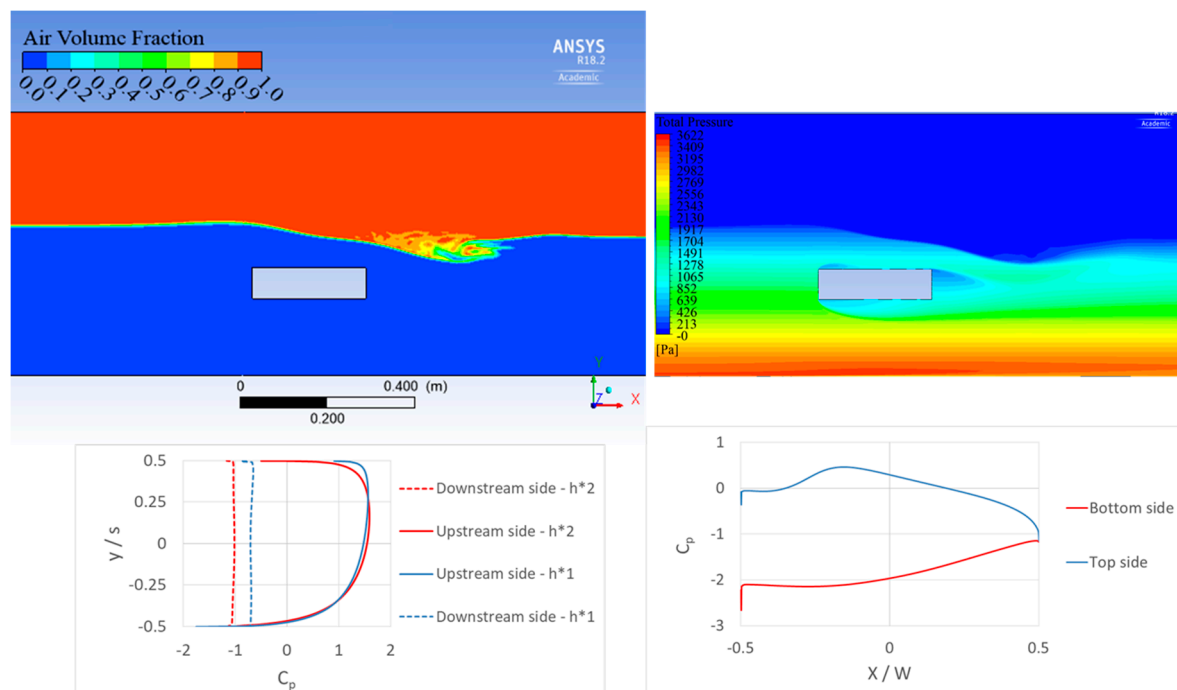


Figure 19. (Top left) Hydraulic jump downstream of the bridge, $h^* = 2$, $Fr_s = 0.97$. (Top right) Total pressure (Pa) in the flow around the deck. (Bottom left) Pressure coefficient on upstream and downstream faces of the deck. (Bottom right) Pressure coefficient on upper and lower faces of the deck.

The pressure distribution on the upstream and downstream faces of the deck can be defined in a non-dimensional form based on the pressure coefficient of Equation (9).

$$C_p = \frac{p - p_0}{\frac{1}{2}\rho U_u^2} \quad (9)$$

where p_0 : Hydrostatic pressure calculated from the simulated water surface level, p : Total pressure, ρ : Water density, and U_u : Upstream velocity.

A higher flow velocity in the hydraulic jump (which occurs at an h^* around 2, but not h^* around 1) results in a higher pressure drop and hence a higher pressure difference between trailing and leading edges of the bridge i.e., higher C_D (Figure 19). As Figure 18 shows, the presence of this hydraulic jump has a significant effect on the drag coefficient.

Scenario 2: Fixed Blockage Ratio

In the previous section, we noticed that the blockage ratio and boundaries (free surface and bottom channel) have an influence on force coefficients. To investigate the effect of boundaries independently, in the second scenario, the water depth is kept constant, $h_u = 0.42$ m, whilst the position of the bridge is changed from almost the bottom of the channel ($h_b = 0.105$ m) to the free surface ($h_b = 0.35$ m). In this way, the blockage ratio will remain constant during all simulations ($Br = 0.17$).

The effect of boundaries on the lift coefficient is shown in Figure 20. When the top of the bridge is located at the free surface ($h^* = 1$), flow separation only occurs at the bottom of the bridge; despite this separation, acceleration of flow under the deck causes a strong downward lift. As the deck approaches the middle of the channel, $3 < h^* < 4$, the flow patterns on the upper and lower parts of the deck become more symmetric and hence lift approaches zero. Once the deck is closer to the bottom of the channel, $h^* > 4$, the flow pattern becomes asymmetric, the detached boundary layer on the bottom side of the deck is forced to reattach to the deck, and higher suction above the deck causes a positive lift coefficient, as shown in Figure 21. Additionally, note that the increasing upstream velocity results in a more negative lift coefficient.

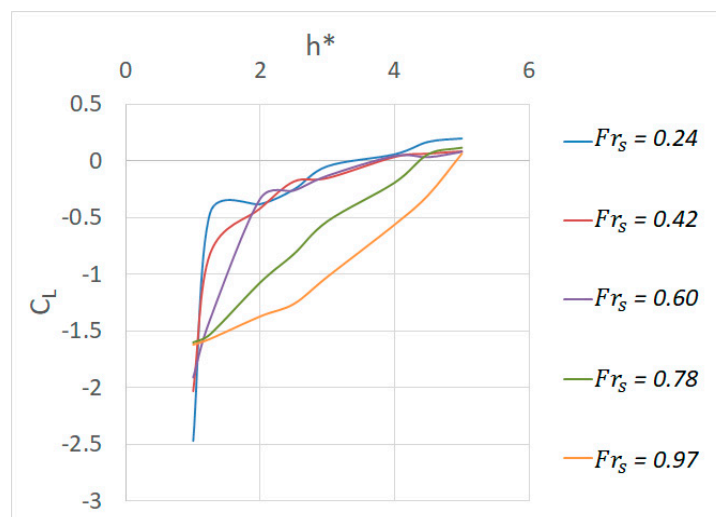


Figure 20. Effect of boundaries (free surface and bottom channel) on the lift coefficient for $h_u/s = 6$.

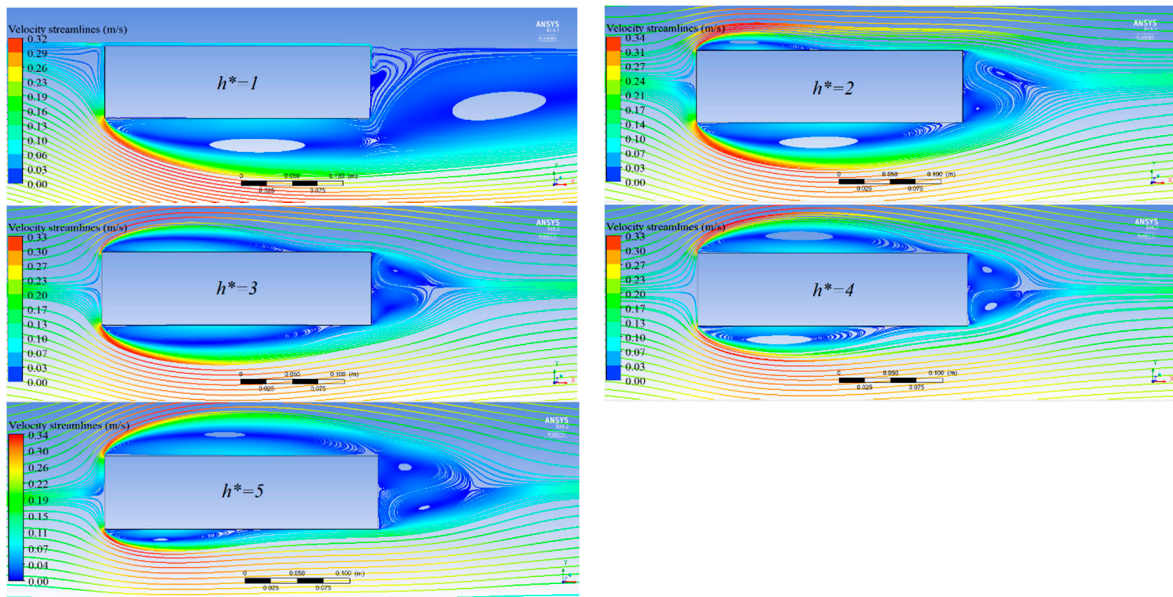


Figure 21. Streamlines of mean velocities around the deck for different inundation ratios, $Fr_s = 0.24$.

Scenario 3: Fixed Inundation Ratio

In the final set of simulations, the submergence ratio was kept constant by changing both the upstream water elevation and distance of the bridge from the channel floor. In this way, the effect of the blockage ratio can be investigated independently of the submergence ratio.

The effect of the blockage ratio on the drag and lift coefficients is quite significant as shown in Figure 22. Regardless of the upstream velocity, an increase in the blockage ratio results in an increase in the drag coefficient. This rise in the drag coefficient is due to both the increase in pressure on the front side and also the increase of negative pressure on the back side of the deck, Figure 23. This fact implies that the constant drag coefficient of 2 to 2.2, which was suggested by Hamill [17], incorrectly neglects the effect of blockage. In fact, for a blockage ratio larger than about 0.25, the drag coefficient is larger than 2.2 regardless of the deck Froude number.

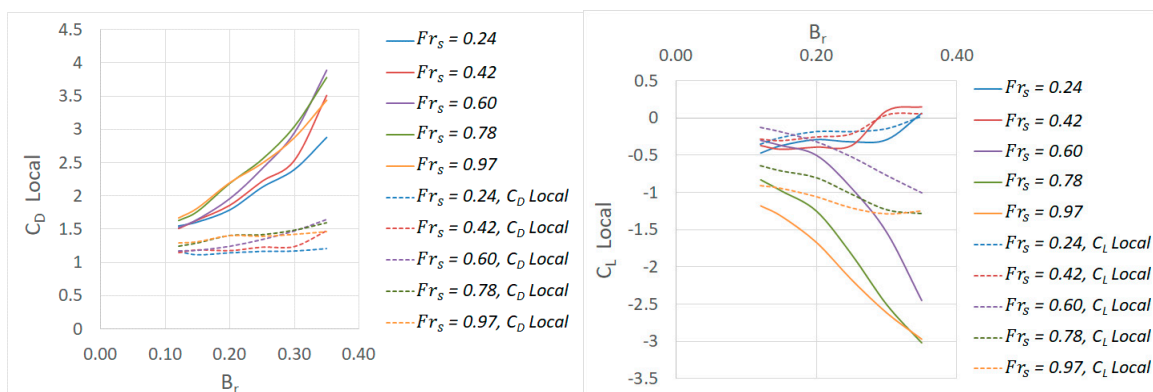


Figure 22. Drag coefficient (left) and lift coefficient (right) versus the blockage ratio. Based on the two scenarios of undisturbed upstream velocity and local velocity (dotted lines). $h^* = 2$.

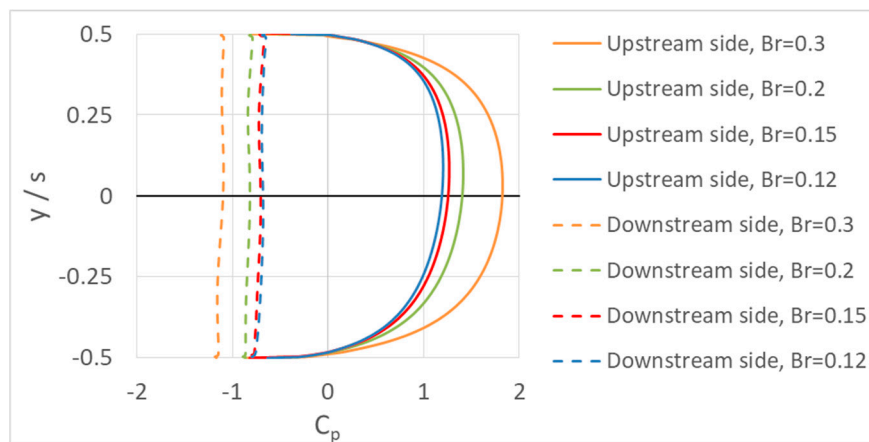


Figure 23. Pressure coefficient in the upstream and downstream side of the deck for different blockage ratios.

On the other hand, a decrease in the blockage ratio shifts the drag coefficient towards the canonical value of 1.6 for a rectangular cylinder in unbounded flow. Therefore, for a blockage ratio of less than 0.15, the drag coefficient asymptotes to a constant value. This point is in agreement with the research of West and Alpert [18] on a circular deck. According to their experimental research on drag forces on a circular deck in bounded flow, when the blockage ratio is between 0.06 to 0.16, the drag coefficient is close to that of unbounded flow i.e., with zero blockage ratio.

Figure 22 shows that an increase in the blockage ratio results in a higher drag coefficient. However, one should note that the drag coefficient was defined based on the undisturbed upstream velocity (U_u). An increase in the blockage ratio also results in a higher local velocity around the bridge. If we recalculate the drag and lift coefficients based on the higher local velocity around the bridge (Figure 22), the steep rise in the drag and lift coefficients with Br becomes much milder. In fact, a significant part of the increase in the drag and lift coefficients by increasing the blockage ratio is due to increase in the local velocity.

These results bring the fundamental question to the general definition of drag and lift coefficients. The drag coefficient in guidelines and design codes, such as Eurocode [5], Australian Bridge Design Standards [7], and AASHTO Bridge Design Specifications [14], is defined based on the upstream velocity (Equation (5)). The main reason for considering the upstream velocity is the fact that form drag is mainly due to the pressure difference between the front and back side of the deck, hence incident upstream velocity is considered to estimate pressure on the front side. The weak point of this approach is the fact that the effect of an increase in the local velocity is incorrectly ignored. Therefore, for calculating the drag coefficient, it is a better approach to consider the local velocity instead of the upstream velocity or incident velocity. The average local velocity can be estimated by the ratio of discharge to the cross-section area of the river as in Parola [8], which applies this drag coefficient to debris dams.

3.2.3. Incipient Failure Analysis

In the previous section, it was shown how the inundation ratio (h^*), proximity ratio (Pr), and blockage ratio (Br) influence hydrodynamic forces on the bridge deck. However, it is not straightforward to understand when bridge failure will occur by considering only force coefficients. In this section, incipient failure analysis is performed to calculate the threshold of bridge deck motion (which is considered the starting point of failure). For this analysis, the rectangular bridge deck analysed above is considered to be a concrete hollow box girder with a 48% void ratio inside the box and a concrete density of 2400 kg/m^3 . Sixty-four simulations were performed to calculate hydrodynamic forces on the bridge deck, via combinations of four Froude numbers (0.3, 0.45, 0.65, 0.8), four inundation ratios (0.5, 1, 2, 3), and four proximity ratios (1.5, 2, 2.5, 3). Hydrodynamic forces

resulting from the numerical simulations were compared with the restoring forces, and failure was defined when the ratio of driving forces divided by resisting forces becomes equal or greater than 1. The resisting force in the horizontal direction is provided by the frictional force. The weight of the deck is the resisting force in the vertical direction. The positive moment, which is caused by the weight of the deck, acts to resist the overturning moment about the heel of the deck. One important factor in terms of resisting forces is the type of bearing, which determines the friction coefficient. Elastomeric bearings, which are one of the most commonly used bearing type, are considered for the incipient failure analysis, with a friction factor of 0.25.

By extracting the starting point of failure for different h^* , Pr , and Froude numbers, contour lines of the threshold of failure can be extracted (Figure 24). For the range of the h^* , Pr , and Froude numbers investigated, no failures resulted due to vertical instability or overturning moment. Horizontal (sliding) instability was the only failure mechanism to occur, and this occurred at inundation ratios of $h^* > 1.2$.

Figure 24 depicts that for Pr higher than 2 (which is common for bridges), by increasing the proximity ratio, failure occurs at a lower h^* . This indicates that the higher the deck is from the channel floor, the more easily the onset of instability will be reached after water rises above the deck. This is because, for a given inundation ratio, a higher proximity ratio equates to a lower blockage ratio, preventing flow contraction, and allowing a lower flow speed under the bridge than in the case of a lower proximity ratio (higher blockage ratio). This reduction in velocity is equivalent to less downward lift force and hence less stability of the deck. However, this does not apply for very a low proximity ratio of $Pr < 2$, as here the deck is so low that friction from the deck and the bed have an effect. Figure 24 also indicates that most of the failure starts to happen in the relatively small range of the blockage ratio between 0.22 to 0.28.

Based on the Eurocode [5], the drag coefficient for a rectangular cross-section deck is 1.44. Using this constant drag coefficient, contour lines for the threshold of failure based on the Eurocode are also shown in Figure 24. Although, for most of the cases analysed, the Eurocode [5] design gives a conservative threshold of failure (mainly due to not considering lift force), for $Fr = 0.3$ and $Pr = 1.5$, the Eurocode fails to be conservative.

Figure 24 relies on assumptions for the deck-pier drag coefficient and the deck weight (material of construction and void fraction). To avoid such assumptions, the drag coefficient can be plotted as a function of the inundation ratio, proximity ratio, and Froude numbers (Figure 25). Except for an inundation ratio of 0.5, the drag coefficient calculated by the numerical simulation is generally higher than the value of 1.44 proposed by the Eurocode. Compared to the Australian Bridge Design code [7], a wider range of drag coefficients are in the acceptable range, however, this design code also fails to be conservative for all proximity ratios evaluated when $h^* = 1$ and $0.3 < Fr < 0.65$. A comparison of drag coefficients between AS5100 [7] and this study for a Froude number of 0.45 is shown in Table 6.

Table 6. Comparison of drag coefficients between AS5100 [7] and this study. Red numbers indicate situations when AS5100 [7] fails to be conservative.

Pr	h^*	CD—AS5100	CD—Numerical
1.5	3	3.35	2.49
2	3	2.9	2.26
2.5	3	2.5	2.14
3	3	2.35	2.06
1.5	2	3.35	2.85
2	2	2.9	2.5
2.5	2	2.5	2.31
3	2	2.35	2.2
1.5	1	2.1	2.7
2	1	1.93	2.3
2.5	1	1.8	2.09
3	1	1.65	1.94

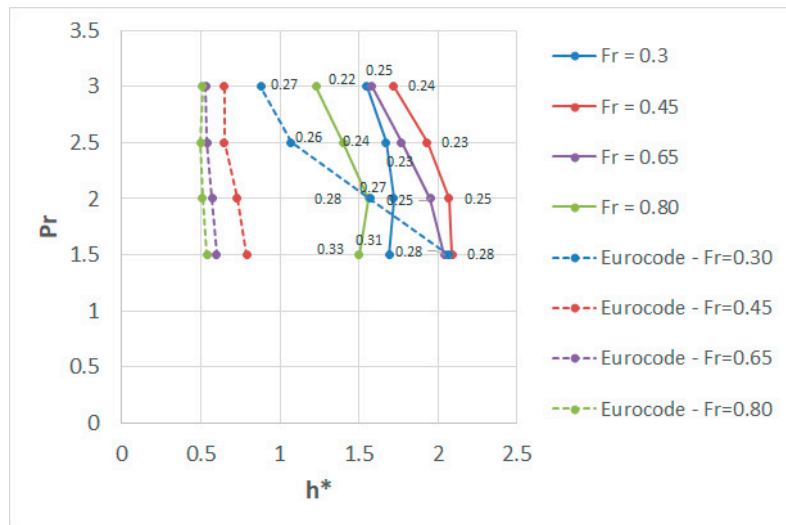


Figure 24. Comparison of contour lines of the threshold of deck failure between the Eurocode ($C_D = 1.44$) [5] and this research for a box deck. Numbers on the figure demonstrate the blockage ratio (Br) for each failure point. To the right of each line is the unstable region, and the stable region is to the left. These stability curves hold for a concrete box girder with a 48% void ratio, an aspect ratio (height:width) of 0.27, and a bearing friction coefficient of 0.25.

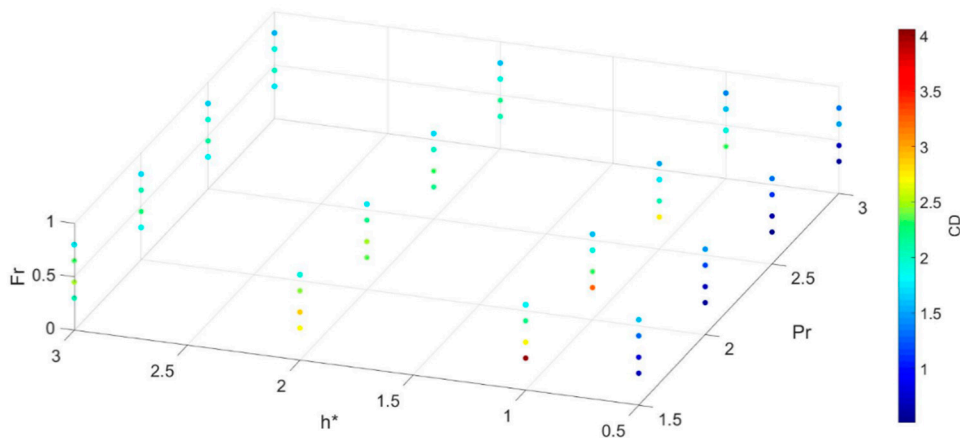


Figure 25. Drag coefficient for box deck based on the proximity ratio ($Pr=1.5,2,2.5,3$), inundation ratio ($h^*=0.5,1,2,3$), and Froude number ($Fr=0.30,0.45,0.65,0.80$). These drag coefficients hold for a rectangular deck with an aspect ratio (height:width) of 0.27.

3.2.4. Countermeasures

In the previous section, it was clarified that when the deck is deeply submerged, sliding failure of the deck is possible due to the lack of frictional resistance to the horizontal flood force. Failure of the bridge deck is affected not only by the severity of the flood, but also by the geometry of the deck. In this section, it is proposed that by adding triangular end caps to the sides of the deck, the stability of the bridge could be increased. To assess this hypothesis, six types of end caps were considered per Figure 26 and Table 7. To investigate the efficiency of each of these end caps in reducing hydrodynamic forces, simulations were performed for each scenario separately.

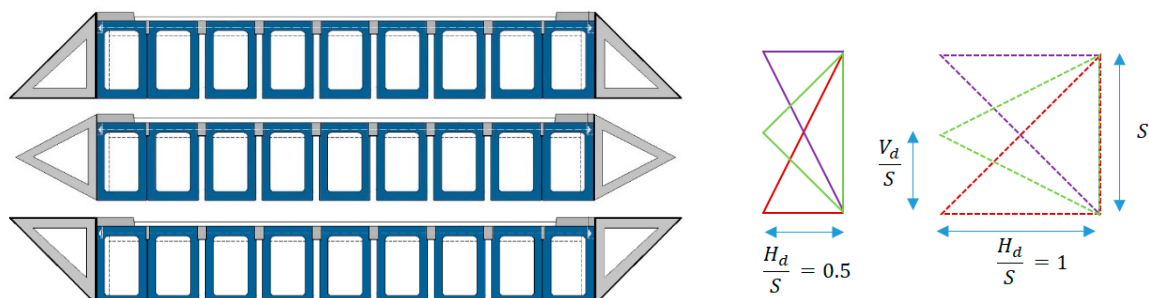


Figure 26. Schematic shape of the deck using end caps for flood force mitigating effect. Displayed on the left are Scenario 6 (top), Scenario 5 (middle), and Scenario 4 (bottom).

Table 7. Dimensions of the end caps.

	Scenario 1	Scenario 2	Scenario 3	Scenario 4	Scenario 5	Scenario 6
$\frac{V_d}{S}$	1	0.5	0	1	0.5	0
$\frac{H_d}{S}$	0.5	0.5	0.5	1	1	1

Figure 27 indicates that for all scenarios (except Scenario 3 with $h^* = 1$), adding end caps to the superstructure results in lower drag force in comparison to the deck without any end caps. However, the magnitude of this reduction in drag force is highly dependent on the profile shape of the end cap. The end cap with a sharp corner at the mid-deck, $\frac{V_d}{S} = 0.5$, results in the lowest drag force. In contrast, the reduction in the drag force is smallest when $\frac{V_d}{S} = 0$. Moreover, regardless of the magnitude of $\frac{V_d}{S}$, an increase of $\frac{H_d}{S}$ amplifies the effect of the end cap, which results in a lower drag force. Here, s is the deck height, V_d is the vertical distance from the deck’s lower chord to the apex of the end cap, and H_d is the horizontal width of the end cap (Figure 26).

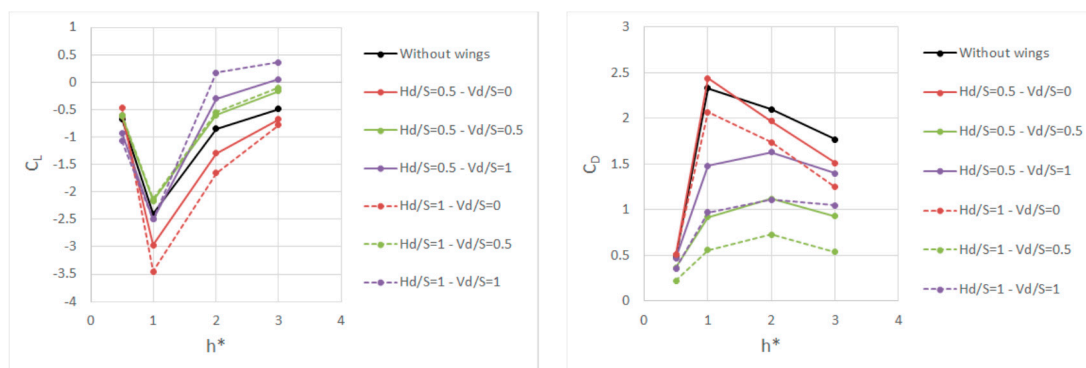


Figure 27. (Left) Lift coefficient versus h^* for six different end caps. ($Pr = 3, Fr = 0.3$). (Right) Drag coefficient versus h^* for six different end caps. ($Pr = 3, Fr = 0.3$).

The influence of end caps on the lift force can also differ based on the shape of the end caps. Generally, whilst the end cap with $\frac{V_d}{S} = 0$ results in a more downward force, other end caps result in less downward force than the deck without any end caps. As with the influence of $\frac{H_d}{S}$ for drag force, an increase of $\frac{H_d}{S}$ amplifies the effect of the end cap, which results in a larger downward force for $\frac{V_d}{S} = 0$, and less downward force for the two other cases. However, the effect of an increase in $\frac{H_d}{S}$ on lift force is not as significant as its effect on drag force. This indicates that lift force is more sensitive to $\frac{V_d}{S}$ than $\frac{H_d}{S}$.

Via incipient failure analysis, it was seen that the failure of the deck due to horizontal force is more probable than failure due to vertical force or an overturning moment. With this in mind, the end cap shape that results in the lowest drag force is most favourable; hence, from the hydrodynamic

perspective, the Scenario 5 end cap type ($\frac{Hd}{s} = 1, \frac{Vd}{s} = 0.5$) can be considered as the most effective type of end cap amongst the six scenarios studied. However, Scenario 5 is not the most economical case as it does not provide a functional use for the bridge’s primary purpose of transportation. Scenario 4 is, therefore, the most practical type of end cap because it reduces the drag force while also providing additional area on top of the deck, which can be used as a pedestrian walkway or cycling lane.

To assess the capability of this countermeasure in extreme hydrodynamic conditions, incipient failure analysis was performed for the deck with the Scenario 5 end cap. By comparing Figure 28 with Figure 24 it can be seen that adding end caps to the deck has resulted in more stability of the deck (each line is shifted to the right). Whilst the simple deck experiences failure between h^* of 1.2 and 2.1 (Figure 24), in the case of the deck with end caps (Scenario 5), failure occurs at higher inundation ratios of up to $h^* = 4.5$ (Figure 28).

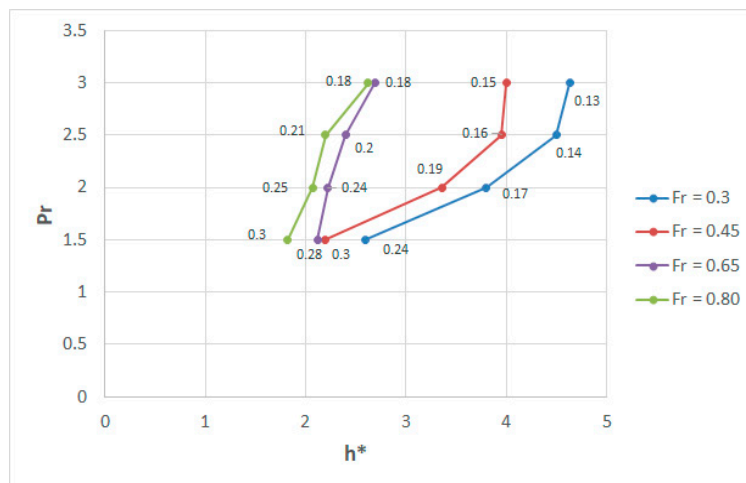


Figure 28. Contour lines of the threshold of failure for Scenario 5 end caps attached to the deck.

3.2.5. Comparison of Flow Patterns and Hydrodynamic Forces on a Box Deck and a Three Girder Deck

Flow patterns and hydrodynamic forces on a box deck (Figure 15) and three girder deck (Figure 29) are compared in this section, as these are two types of common bridge decks, and stability in floods can be one criterion (of many) used in the choice of deck type for a project. Figure 30 indicates that the trends of force and moment coefficients are quite comparable for these two cases. However, the magnitude of these coefficients differs substantially.

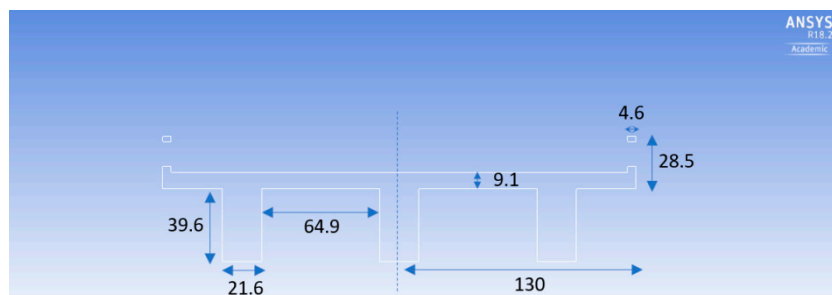


Figure 29. Dimensions of three girder deck in mm.

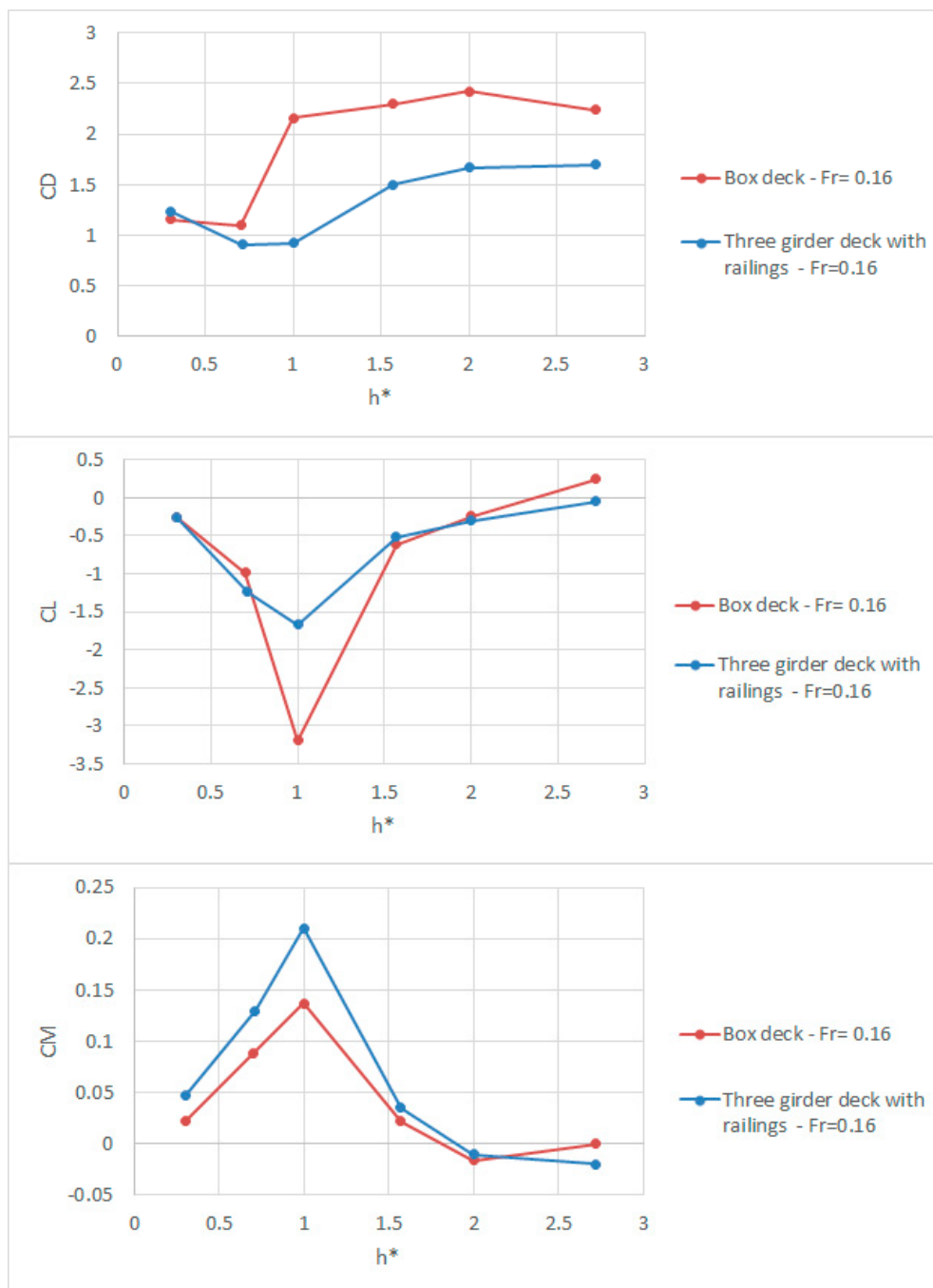


Figure 30. Comparison of force and centroidal moment coefficients between the box deck and three girder deck.

The flow pattern around the deck is significantly different for each geometry (Figure 31). A wider wake area with bigger eddies on the trailing side of the box deck results in lower pressure and, subsequently, a higher drag force. Moreover, a small recirculation zone in front of the upper part of the first girder results in a lower average positive pressure on the leading edge of the girder deck (Figure 32). It should be noted that the frontal area of these two cases are not the same (the three girder deck has a smaller frontal area due to the presence of the railings).

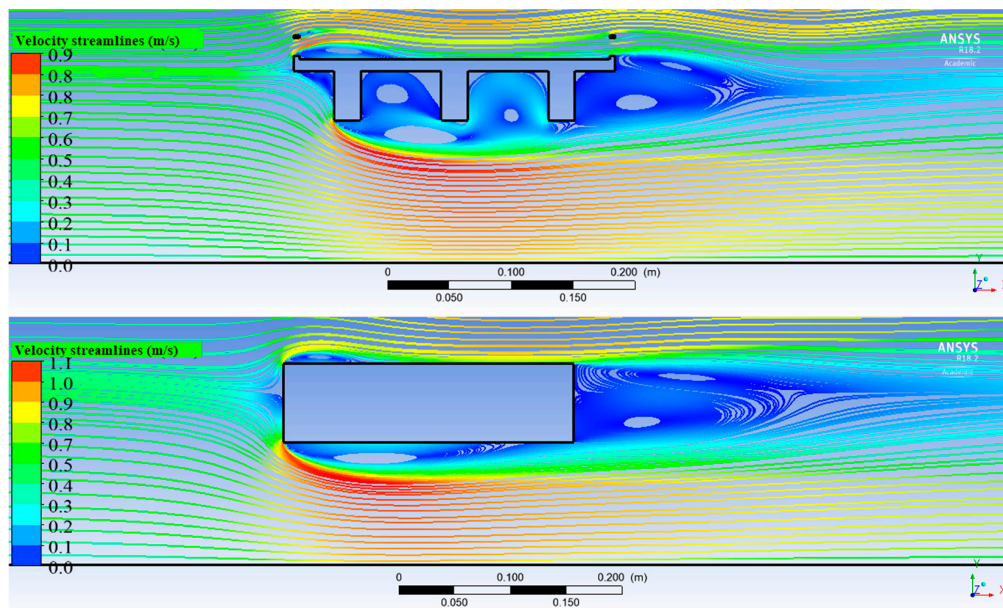


Figure 31. Streamlines of mean velocities around the box deck and three girder deck, $Fr = 0.32$, $Pr = 1.5$, $h^* = 2$.

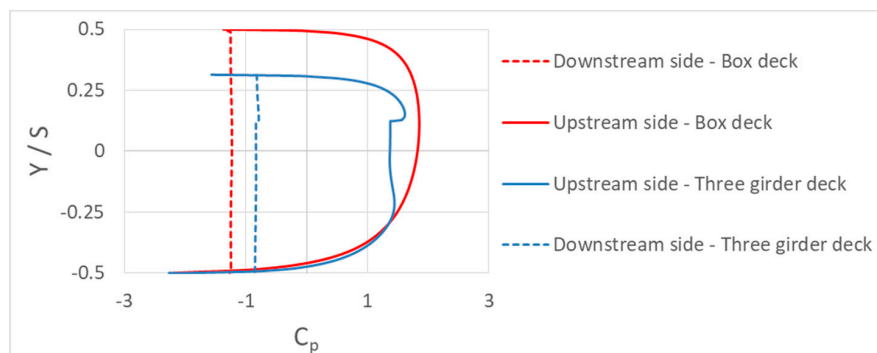


Figure 32. Comparison of the pressure coefficient between the box deck and three girder deck, $Fr = 0.32$, $h^* = 2$.

4. Discussion

The most noteworthy result of the laboratory experiments is that the deck-pier system never failed as a unit. Failure of piers only occurred after the deck failed first (with or without debris), followed by an excessive amount of debris damming on the piers, causing pier overturning. This is an important result because it indicates that hydrodynamic bridge failure can be prevented by strengthening the deck-pier connection to prevent liftoff of the deck from the piers. By keeping the deck attached to the pier, deck failure is prevented because the weight of the pier contributes to holding the deck down, while pier failure is prevented because the downward lift induced by the presence of the deck is strong enough to prevent pier toppling, even in cases with excessive debris damming.

The presence of debris played a significant role in the failure of the bridge. According to the results, a bridge deck can fail without debris accumulations, albeit only at deep inundation ratios. Addition of debris into the system moves this range of conditions at which the bridge deck is dislocated from the pier to a much milder regime. Furthermore, the presence of debris affects bridge stability via both additional lift and additional drag. Moreover, collapse of the pier was only observed when simulated debris was introduced into the experiment. Even with excessive debris present, the collapse of a rigidly connected deck-pier system never occurred, indicating that the strengthened connection here is an effective countermeasure to either deck or pier failure.

Detailed numerical simulations of a bridge deck highlighted the role that flow contraction plays at high blockage ratios. Since the deck drag coefficient is parameterized based on the upstream flow

speed, high blockage causes flow contraction and thereby increased flow speed near the deck, resulting in high drag coefficients. However, this can be addressed by accounting for the blockage ratio in the definition of the drag coefficient. Another physical phenomenon that causes a larger than expected drag coefficient is the presence of supercritical flow above the deck and corresponding hydraulic jump downstream of the deck's trailing edge at inundation ratios near $h^* = 2$. This causes a local maximum in the drag coefficient at high Froude numbers.

Simulations of the threshold of instability of a concrete box girder deck showed that the Eurocode [5] is conservative in most cases because it neglects the negative lift normally acting as a stabilizing force. Nonetheless, in some situations, the code is non-conservative in predicting the threshold of motion. Generalizing further to a rectangular deck, the drag coefficient suggested by the code is non-conservative in all cases where the deck is fully submerged ($h^* > 1$).

Comparison of a box deck with a three-girder deck show that the box deck experiences greater drag than the girder deck because of a larger wake zone in its lee. However, this same bluntness of the box deck causes greater flow blockage than the girder deck causes. The greater flow blockage of the box deck results in a larger negative lift on the box deck than the girder deck. Therefore, overall deck stability will depend on the friction coefficient of the bearings used.

Finally, end caps were proposed for giving decks more stability in general. End caps shaped like right triangles can both reduce the deck drag coefficient and provide additional area on the deck for use as a pedestrian or bicycle lane. Combined with the knowledge gained from the laboratory experiments that tying decks down to the piers will prevent failure, practical countermeasures to hydrodynamic bridge failure can be implemented. For further details of the laboratory experiments and numerical simulations, see [12] and [13], respectively.

5. Conclusions

Laboratory experiments and numerical simulations were carried out to investigate the hydrodynamic failure of bridge decks and piers, the latter especially applicable to piers founded upon spread footings on bedrock. For the specific geometry of the Yabitsu Bridge, experiments showed that failure of a rigidly combined deck-pier system did not occur, even in the presence of excessive debris damming. This indicates that one effective countermeasure to hydrodynamic failure of both decks and piers is a robust connection between these units. To resist sliding of the deck, this can take the form of shear keys or unseating prevention devices, which are common on piers in earthquake prone areas [2]. To resist the overturning moment as well, chains or shear keys with vertical interlocking could be used, as long as these are anchored in both the deck and pier well enough to prevent pull-out failure when subject to tension. The reason for the increased stability of the robustly connected deck-pier system is because the weight of the pier helps prevent the deck from sliding or overturning, while the presence of the deck causes a downward lift force on the deck-pier system, which functions to keep the piers upright as well.

Another countermeasure to deck failure (and therefore to failure of the deck-pier unit) is inclusion of end caps on the leading and trailing edges of the deck. These function to reduce the deck drag coefficient by shifting the deck away from a blunt body flow regime to a more streamlined regime, and further play a practical role by functioning as bicycle or pedestrian lanes atop the deck. However, this countermeasure needs to be further evaluated when exposed to debris, as the reduction in drag might be nullified by debris damming, while the buoyancy of the debris itself might exacerbate lift on the deck even more than in the case without end caps. Also, T-girder decks were found to be more stable than box girder decks because the T-girders are less blunt than the box girders, and also experience less buoyancy.

Importantly, both sets of experiments found that existing design guidelines for bridges subject to hydrodynamic forces are non-conservative in some regimes, especially those for which free surface effects are important, those with the bridge deeply submerged, or those with a high blockage ratio. For these cases, the results presented in this paper will be useful to designers, but work needs to be done to generalize the results for a greater range of bridge deck and pier geometries.

Author Contributions: Conceptualization, J.D.B.; investigation, K.O. and N.N.; resources, S.M.; writing—original draft preparation, K.O, N.N., and J.D.B.; writing—review and editing, J.D.B.; supervision, J.D.B., Y.Y., C.v.d.V., S.N.J., and W.U.

Funding: This research was partially funded by the Delta Infrastructure and Mobility Initiative (DIMI) of TU Delft, and by the Netherlands Organization for Scientific Research (NWO) TTW SAFElevee project (#13861).

Acknowledgments: We are grateful to Ian Turner of the University of New South Wales for providing the Australian Bridge Design Code.

Conflicts of Interest: The authors declare no conflict of interest. The funders had no role in the design of the study; in the collection, analyses, or interpretation of data; in the writing of the manuscript, or in the decision to publish the results.

References

1. Flint, M.M.; Fringer, O.; Billington, S.L.; Freyberg, D.; Diffenbaugh, N.S. Historical Analysis of Hydraulic Bridge Collapses in the Continental United States. *J. Infrastruct. Syst.* **2017**, *23*, 04017005. [CrossRef]
2. Bricker, J.D.; Nakayama, A. Contribution of trapped air, deck superelevation, and nearby structures to bridge deck failure during a tsunami. *J. Hydraulic Eng.* **2014**, *140*, 05014002. [CrossRef]
3. Bricker, J.D.; Nakayama, A.; Takagi, H.; Mitsui, J.; Miki, T. Mechanisms of Damage to Coastal Structures due to the 2011 Great East Japan Tsunami. In *Handbook of Coastal Disaster Mitigation for Engineers and Planners*; Esteban, M., Takagi, H., Shibayama, T., Eds.; Elsevier: Amsterdam, The Netherlands, 2015; pp. 385–415.
4. Richardson, E.V.; Davis, S.R. *Evaluating Scour at Bridges*; Hydraulic Engineering Circular No. 18; Federal Highway Administration: Washington, DC, USA, 2001.
5. EU. EN 1991-1-6: Eurocode 1: Actions on Structures—Part 1–6: General Actions—Actions during Execution; Authority: The European Union per Regulation 305/2011, Directive 98/34/EC, Directive 2004/18/EC; EU: Brussels, Belgium, 2005.
6. Kerenyi, K.; Sofu, T.; Guo, J. *Hydrodynamic Forces on Inundated Bridge Decks*; Report FHWA-HRT-09-028 of the Federal Highway Administration; Federal Highway Administration: Washington, DC, USA, 2009.
7. *Australian Bridge Design Code*; Standards Australia International Ltd.: Sydney, Australia, 2004.
8. Parola, A.C. *Debris Forces on Highway Bridges. National Cooperative Highway Research Program*; National Academy Press: Washington, DC, USA, 2000.
9. Malavasi, S.; Guadagnini, A. Hydrodynamic Loading on River Bridges. *J. Hydraulic Eng.* **2003**, *129*, 854–861. [CrossRef]
10. Jempson, M.A. Flood and Debris Loads on Bridges. Ph.D. Thesis, University of Queensland, Brisbane, Australia, 2000.
11. Trelleborg Engineered Products: Elastomeric Bearing Pads & Strips. Available online: <https://www.trelleborg.com/engineered-products/~media/engineered> (accessed on 18 May 2018).
12. Oudenbroek, K. Experimental Research on Hydrodynamic Failure of River Bridges on Spread Footings. Master's Thesis, Delft University of Technology, Delft, The Netherlands, 2018.
13. Naderi, N. Numerical Simulation of Hydrodynamic Forces on Bridge Decks. Master's Thesis, Delft University of Technology, Delft, The Netherlands, 2018.
14. American Association of State Highway and Transportation Officials. *AASHTO LRFD Bridge Design Specifications*; American Association of State Highway and Transportation Officials: Washington, DC, USA, 2013.
15. Ducrocq, T. Flow and drag force around a free surface piercing cylinder for environmental applications. *Environ. Fluid Mech.* **2017**, *17*, 629–645. [CrossRef]
16. Yu, D.; Kareem, A. Two-dimensional simulation of flow around rectangular prisms. *J. Wind Eng. Ind. Aerodyn.* **1996**, *62*, 131–161. [CrossRef]
17. Hamill, L. *Bridge Hydraulics*; E & FN Spon: London, UK, 1999; p. 344.
18. West, G.S.; Apelt, C.J. Measurements of fluctuating pressures and forces on a circular cylinder in the Reynolds number range 10^4 to 2.5×10^5 . *J. Fluids Struct.* **1993**, *7*, 227–244. [CrossRef]

